Int. J. Heat Mass Transfer. Vol. 35, No. 10, pp. 2357–2365, 1992
Printed in Great Britain

0017–9310/92 $5.00 + 0.00
Pergamon Press Ltd

Calculation of a circular jet in crossflow with a multiple-time-scale turbulence model

S.-W. KIM and T. J. BENSON
NASA/Lewis Research Center, MS 5-11, Cleveland, OH 44135, U.S.A.

(*Received* 15 *May* 1991 *and in final form* 8 *November* 1991)

Abstract—Calculation of a three-dimensional turbulent flow of a jet in a crossflow using a multiple-time-scale turbulence model is presented. The turbulence in the forward region of the jet is in a stronger non-equilibrium state than that in the wake region of the jet, while the turbulence level in the wake region is higher than that in the front region. The calculated flow and the concentration fields are in very good agreement with the measured data, and it indicates that the turbulent transport of mass, concentration and momentum is strongly governed by the non-equilibrium turbulence. The capability of the multiple-time-scale turbulence model to resolve the non-equilibrium turbulence field is also discussed.

INTRODUCTION

JETS IN crossflows can be found in a number of engineering applications. For example, in gas turbine combustors, circumferentially distributed jets are used to ensure correct combustion in the flame zone and then to dilute the hot gas entering the turbine. Various experimental and numerical investigations of jets in crossflows have been made to better understand turbulent flows in such engineering applications. Compilations of various experimental investigations of jets in crossflows can be found in Crabb *et al.* [1] and Khan [2] and that of numerical investigations can be found in Claus and Vanka [3].

It can be found in ref. [3] that the numerical results obtained by various investigators using k–ε turbulence models exhibit improved comparison with the measured data in some parts of the flow domain and worse agreement with the measured data in other parts as the mesh is refined. Claus and Vanka [3] carried out a grid independence study of a row of jets in a crossflow and showed that the deteriorated comparison is caused by the inability of the k–ε turbulence models to describe the complex turbulence field. In previous numerical simulations, the upstream region of the jet was excluded from the computational domain. Andreopoulos [4] showed, however, that the jet and the crossflow interact strongly with each other at the jet exit and that the influence is propagated toward the upstream region of the jet. The deteriorated numerical results can thus also be caused by the numerical models which cannot fully account for the strong interaction at the jet exit. In the present study, the boundary for the circular jet is located at one diameter upstream of the jet exit so that the strong interaction at the jet exit is also accurately simulated.

Numerical results for various complex turbulent flows (e.g. turbulent flows subjected to extra strains caused by streamline curvature, interaction of multiple number of shear layers, and shock wave-boundary layer interactions) obtained using two-equation turbulence models, algebraic Reynolds stress turbulence models (ARSM) and Reynolds stress turbulence models (RSM) show that these turbulence models cannot accurately describe the turbulence fields of various complex turbulent flows [5]. One common inability of the two-equation turbulence models, ARSM and RSM, is that these turbulence models cannot account for 'non-equilibrium turbulence' due to the use of a single time scale to describe both the turbulent transport and the dissipation of the turbulent kinetic energy. The 'non-equilibrium turbulence' is explained in the 'Analysis' section. On the other hand, it can be seen in refs. [6–8] and the references cited therein that the numerical results for various complex turbulent flows obtained using the multiple-time-scale turbulence model (hereafter abbreviated as the MS turbulence model) are in as good agreement with the measured data as those obtained using an optimized k–ε, ARSM, or RSM turbulence model for each flow case. The capability of the MS turbulence model to solve widely different complex turbulent flows is attributed to its capability to resolve the non-equilibrium turbulence.

The Reynolds averaged Navier–Stokes equations, the concentration equation, and the turbulence equations are solved by a finite volume method that incorporates a pressure-staggered mesh and a partial differential equation for incremental pressure [9]. Details of the numerical method and calculations of a three-dimensional lid-driven cavity flow and a laminar flow through a 90°-bend square duct can be found in ref. [9]. It is shown in the reference that the present method yields a grid independent solution for the

NOMENCLATURE

c	normalized concentration
$c_{\varepsilon i}$	model constants for ε_p equation ($i = 1, 3$)
c_{ti}	model constants for ε_t equation ($i = 1, 3$)
c_μ	eddy viscosity coefficient
$c_{\mu f}$	constant coefficient ($=0.09$)
D	diameter of circular jet
k	turbulent kinetic energy ($k = k_p + k_t$)
k_p	turbulent kinetic energy in production range
k_t	turbulent kinetic energy in dissipation range
p	pressure
P_r	production rate
u_j	time averaged velocity ($=\{u, v, w\}$)
U_0	free-stream velocity of crossflow
W_j	jet velocity averaged across jet cross-section
x_j	spatial coordinates ($=\{x, y, z\}$)
y^+	wall coordinate based on friction velocity.

Greek symbols

ε_p	energy transfer rate
ε_t	dissipation rate
μ	molecular viscosity
μ_d	molecular diffusivity
μ_t	turbulent viscosity
ρ	density
σ_d	turbulent Schmidt number
σ_i	turbulent Prandtl number for i-equation, $i = \{k_p, \varepsilon_p, k_t, \varepsilon_t\}$.

separated three-dimensional curved duct flow with as small as $68 \times 18 \times 33$ grid points and that the numerical results are in excellent agreement with the measured data.

ANALYSIS

The anisotropy of the turbulence is the most easily detectable phenomenon in a measurement of a turbulent flow, thus, it was conceived that the poor capability of the two-equation turbulence models to resolve complex turbulent flows is attributed to the inability of the turbulence models to account for the anisotropy of the turbulence. The emphasis was thus laid upon improving the ARSM and the RSM. A number of numerical investigations carried out during the last one-and-a-half decades show that the ARSM and RSM still cannot accurately predict the turbulence phenomena occurring in various flows unless the pressure–strain rate correlation is optimized for each flow [7, 8].

A careful examination of semi-empirical data (theoretically derived data from a set of measured data) reveals that the non-equilibrium turbulence also influences the developments of the mean flow field and the turbulence field. Here, the 'non-equilibrium turbulence' represents the state of a turbulence field in which P_r/ε_t varies rapidly in space so that the shape and the frequency domain of the spectral density varies widely in space. The spectral density curves shown in Fig. 1 are constructed based on the measured data of Klebanoff [10] and Wygnanski and Fiedler [11]. It can be seen in Fig. 1 that the energy-containing large eddies generated by the instability of the mean fluid motion are characterized by low frequency and the fine scale eddies in the dissipation range are characterized by high frequency, thus the cascade process of the turbulent kinetic energy is also implicitly described in the figure. The influence of the non-equilibrium turbulence and the capability of the MS turbulence model to resolve the non-equilibrium turbulence phenomena is described below.

The convection–diffusion equations of the MS turbulence models describe the physically observed turbulence phenomena most naturally in the sense that the turbulent transport of mass and momentum is described using the time scale of large eddies and the dissipation rate is described using the time scale of fine-scale eddies [6–8, 12]. The turbulent kinetic energy and the energy transfer rate equations for energy containing large eddies are given as

$$\frac{\partial}{\partial x_j}(\rho u_j k_p) - \frac{\partial}{\partial x_j}\left[\left(\mu + \frac{\mu_t}{\sigma_{kp}}\right)\frac{\partial k_p}{\partial x_j}\right] = \rho P_r - \rho \varepsilon_p \tag{1}$$

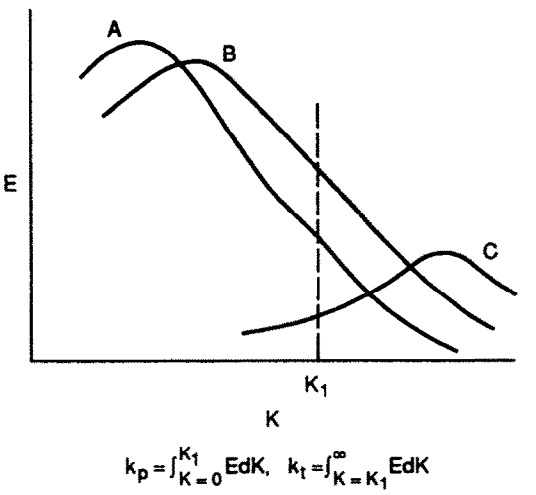

FIG. 1. Spectral density for non-equilibrium turbulent flows, A: maximum shear location in a circular jet ($P_r/\varepsilon_t > 1$) [11], B: equilibrium region ($P_r/\varepsilon_t \approx 1$), C: free stream region of a boundary layer flow ($P_r \approx 0$) [10].

$$\frac{\partial}{\partial x_j}(\rho u_j \varepsilon_p) - \frac{\partial}{\partial x_j}\left[\left(\mu + \frac{\mu_t}{\sigma_{\varepsilon p}}\right)\frac{\partial \varepsilon_p}{\partial x_j}\right] = \frac{\rho}{k_p}(c_{p1}P_r^2 + c_{p2}P_r\varepsilon_p - c_{p3}\varepsilon_p^2) \quad (2)$$

where the production rate (P_r) is given as

$$P_r = \frac{\mu_t}{\rho}\left[2\left(\frac{\partial u}{\partial x}\right)^2 + 2\left(\frac{\partial v}{\partial y}\right)^2 + 2\left(\frac{\partial w}{\partial z}\right)^2 + \left(\frac{\partial u}{\partial y} + \frac{\partial v}{\partial x}\right)^2 + \left(\frac{\partial u}{\partial z} + \frac{\partial w}{\partial x}\right)^2 + \left(\frac{\partial v}{\partial z} + \frac{\partial w}{\partial y}\right)^2\right]$$

and repeated indices imply summation over the index unless otherwise stated. The turbulent kinetic energy and the dissipation rate equations for fine scale eddies are given as

$$\frac{\partial}{\partial x_j}(\rho u_j k_t) - \frac{\partial}{\partial x_j}\left[\left(\mu + \frac{\mu_t}{\sigma_{kt}}\right)\frac{\partial k_t}{\partial x_j}\right] = \rho\varepsilon_p - \rho\varepsilon_t \quad (3)$$

$$\frac{\partial}{\partial x_j}(\rho u_j \varepsilon_t) - \frac{\partial}{\partial x_j}\left[\left(\mu + \frac{\mu_t}{\sigma_{\varepsilon t}}\right)\frac{\partial \varepsilon_t}{\partial x_j}\right] = \frac{\rho}{k_t}(c_{t1}\varepsilon_p^2 + c_{t2}\varepsilon_p\varepsilon_t - c_{t3}\varepsilon_t^2) \quad (4)$$

and the eddy viscosity is given as

$$\mu_t = \rho c_{\mu f}\frac{k^2}{\varepsilon_p}. \quad (5)$$

The turbulence model constants are given as; $\sigma_{kp} = 0.75$, $\sigma_{kt} = 0.75$, $\sigma_{\varepsilon p} = 1.15$, $\sigma_{\varepsilon t} = 1.15$, $c_{p1} = 0.21$, $c_{p2} = 1.24$, $c_{p3} = 1.84$, $c_{t1} = 0.29$, $c_{t2} = 1.28$, and $c_{t3} = 1.66$.

The capability of the MS turbulence model to resolve the non-equilibrium turbulence depends largely on the load functions of the ε_p and ε_t equations and the way the turbulence model constants are established. The load functions of the ε_p and ε_t equations are obtained from a physical dimensional analysis [6], and the establishment of the model constants are based on the assumptions that the turbulence field of a uniformly sheared flow can approach an asymptotic state in which P_r/ε_t becomes a constant and that the ratio of $\varepsilon_t/\varepsilon_p$ depends on the ratio of P_r/ε_t. The first assumption that such an asymptotic state can exist is shown in Tavoularis and Karnik [13]. In such asymptotic states of uniformly sheared flows, the diffusion term vanishes, and the asymptotic ratio of k_p/k_t can be obtained by dividing equation (1) by equation (3), i.e.

$$\frac{k_p}{k_t} = \frac{Dk_p}{Dk_t} = \frac{P_r/\varepsilon_t - \varepsilon_p/\varepsilon_t}{\varepsilon_p/\varepsilon_t - 1}. \quad (6)$$

It can be seen in equation (6) that the existence of the asymptotic ratio of k_p/k_t depends on the realizability of the second assumption that the ratio of $\varepsilon_t/\varepsilon_p$ depends on the ratio of P_r/ε_t. The second assumption can be verified by numerical results posterily, or it can be verified indirectly by comparing the MS eddy viscosity equation with that of the generalized algebraic stress turbulence models [14–16].

The semi-empirical c_μ for a plane jet obtained by Rodi [14] and the c_μ curves used in the generalized algebraic stress turbulence models of Launder [15] and Kim and Chen [16] are shown in Fig. 2. It can be seen in the figure that c_μ is decreased as P_r/ε_t is increased, and c_μ is increased as P_r/ε_t is decreased. The eddy viscosity equation, equation (5), can be rewritten in a form comparable with that of the generalized algebraic stress turbulence models, i.e.

$$\mu_t = \rho c_\mu \frac{k^2}{\varepsilon_t} \quad (7)$$

where $c_\mu = c_{\mu f}(\varepsilon_t/\varepsilon_p)$ and $\varepsilon_t/\varepsilon_p$ is a function of P_r/ε_t as shown in Fig. 2, thus the second assumption is justified within the context of the generalized algebraic stress turbulence models. It can be seen in equation (7) that the spatially varying eddy viscosity coefficient depends on the local non-equilibrium turbulence. As a remark, the generalized algebraic stress turbulence models yield accurate numerical results for shear layers when used in boundary layer flow solvers. The use of these turbulence models in elliptic (two-dimensional) flow solvers does not, however, easily yield a converged solution due to a severe interpolation used in the c_μ function. Furthermore, the generalized algebraic stress turbulence models lack many features of the MS turbulence model.

The three non-equilibrium turbulence levels (points A, B, and C) imbedded into the MS turbulence equation are also shown in Fig. 2. The measured data that corresponds to the point A (i.e. $P_r/\varepsilon_t = 1.5$) can be found in Tavoularis and Karnik [13]. For point A,

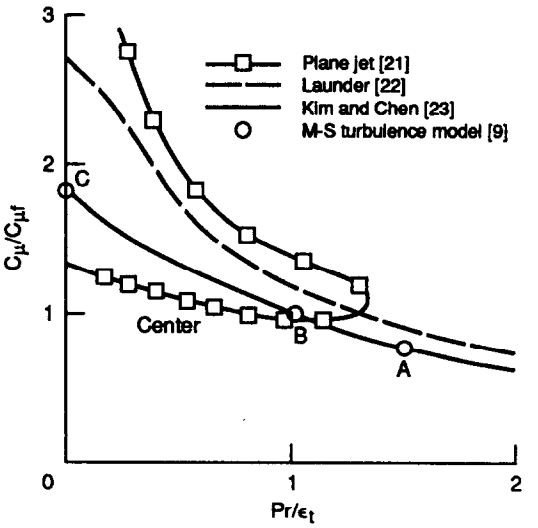

FIG. 2. $c_\mu/c_{\mu f}$ ($= \varepsilon_t/\varepsilon_p$) profiles, A: $P_r/\varepsilon_t > 1$, B: $P_r/\varepsilon_t \approx 1$, C: $P_r \approx 0$.

the value of $\varepsilon_t/\varepsilon_p \approx 0.95$ can be estimated from Fig. 2 and equation (6) yields $k_p/k_t \approx 9.0$. For turbulent flows in an equilibrium state (point B), $P_r = \varepsilon_t$, and ε_p has to be equal to both of them to maintain the equilibrium state. In this case, equation (6) becomes indeterminate; and the ratio of $k_p/k_t \approx 4.0$ can be obtained from a near-wall analysis of turbulent flows in equilibrium state [6]. In the free stream region of turbulent flows (point C), the production rate vanishes. In this case, the ratio of $\varepsilon_t/\varepsilon_p \approx 2.5$ can be estimated from Fig. 2 and equation (6) yields $k_p/k_t \approx 0.7$. The three ratios of k_p/k_t obtained in the analysis show that $(k_p/k_t)_A > (k_p/k_t)_B > (k_p/k_t)_C$. The implication of this inequality is also illustrated in Fig. 1, where the frequency domain is divided into two parts by a simplified split spectrum [6, 12]. It can be seen in the figure that the ratio of k_p/k_t is determined by the shape and the frequency domain of each spectral density curve and that the variation of k_p/k_t is in agreement with the theoretical analysis.

Calculations of various boundary layer flows using the MS turbulence model always reproduce the imbedded non-equilibrium turbulence states. For highly complex turbulent flows, large eddies (characterized by a large value of k_p/k_t) generated in the upstream region are convected in the downstream direction. In such downstream regions, the relationship between P_r/ε_t and $\varepsilon_t/\varepsilon_p$ is influenced by the convected eddies and the numerical results exhibit the trend of imbedded non-equilibrium turbulence.

The convection–diffusion equation for the concentration is given as

$$\frac{\partial}{\partial x_j}(\rho u_j c) - \frac{\partial}{\partial x_j}\left[\left(\mu_d + \frac{\mu_t}{\sigma_d}\right)\frac{\partial c}{\partial x_j}\right] = 0 \qquad (8)$$

where $\sigma_d = 0.75$ is used in the present study. Due to the strong large eddy mixing, the molecular diffusivity can be ignored or formally approximated as $\mu_d = \mu/\sigma_d$; and neither of the approximations influence the numerical results significantly. In the experiment [1], the concentration field was measured by injecting helium gas (He) into the circular jet. The concentration of the helium is one percent of the air–helium mixture at the jet inlet, and hence the concentration equation, equation (8), is solved uncoupled from the momentum equations.

NUMERICAL RESULTS

The circular jet in a uniform crossflow [1] considered in the present study is schematically shown in Fig. 3 where $D = 0.0254$ m, $U_0 = 12$ m s^{-1} and $W_j = 27.6$ m s^{-1}. The computational domain is also described in the figure and $(x, y, z) = (0, 0, 0)$ refers to the center of the jet exit. The north ($y = 3.1D$ plane) and top ($z = 7.5D$ plane) boundaries are located sufficiently far away from the jet exit so that the numerical results near the jet exit are not significantly influenced by the far field boundary conditions. The

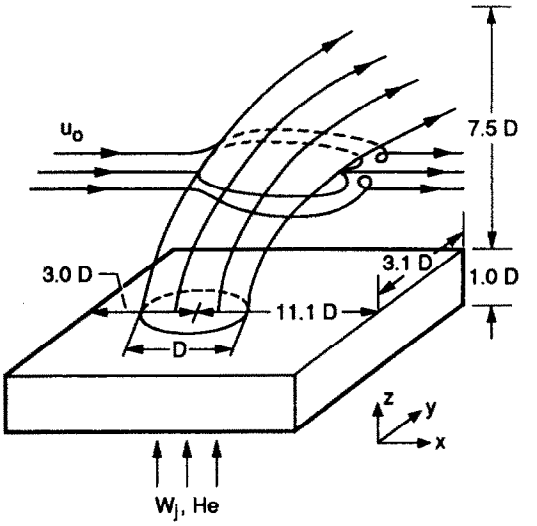

FIG. 3. Nomenclature and computational domain for a circular jet in crossflow.

symmetric half of the flow domain is discretized by $148 \times 61 \times 94$ grid points in x-, y-, and z-coordinate directions, respectively. The body-fitted grid near the jet exit is shown in Fig. 4. The smallest mesh size in the direction normal to the wall is 0.6×10^{-4} m ($y^+ \approx 1.5$ based on the inlet boundary conditions of the jet) and this mesh size is sufficiently small to resolve the near-wall turbulence field in the vicinity of the jet exit. The largest mesh size used near the far field boundaries is approximately half of the jet diameter.

The inlet boundary conditions for the crossflow are obtained from measured data for a fully developed

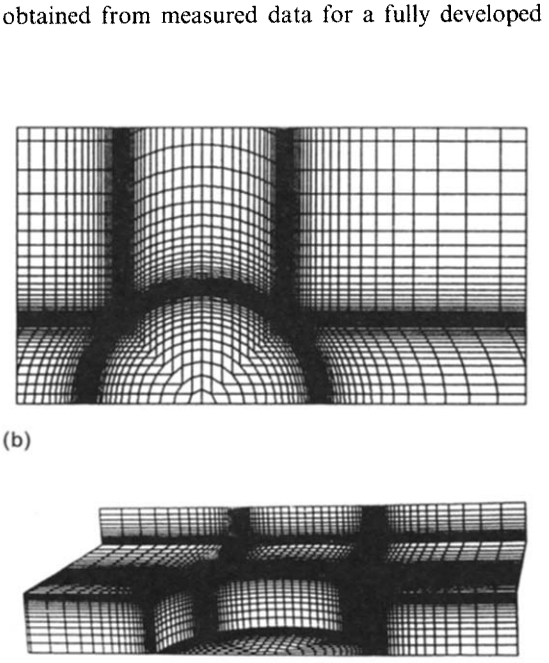

FIG. 4. Mesh in the vicinity of jet exit, (a) top view, (b) perspective view.

boundary layer flow over a flat plate [10]. The non-dimensional velocity and the turbulent kinetic energy profiles are scaled to yield a boundary layer thickness of 0.005 m at the inlet boundary. The ratios of k_p/k_t and $\varepsilon_p/\varepsilon_t$ are estimated based on the ratio of P_r/ε_t [6]. The no-slip boundary condition for velocities, vanishing gradient for concentration, and vanishing turbulent kinetic energy are prescribed at the solid wall boundary. A vanishing gradient boundary condition is used for all flow variables at the exit boundary ($x = 11.1D$ plane) and on the symmetry boundary ($y = 0$ plane). The free stream boundary condition is used on the north and the top boundaries. A fully developed pipe flow and constant concentration ($c = 1.0$) conditions are prescribed at the jet inlet boundary. The near-wall turbulence is described by a 'partially low Reynolds number' near-wall turbulence model [17]. The converged solution is obtained in approximately 1200 iterations, and the imbalances of the mass and concentration leaving the flow domain with respect to those entering the flow domain are less than 0.0025% and 0.95%, respectively.

The contour plots of the jet velocity, the pressure, and the total pressure at the jet exit are shown in Fig. 5, where the increments between the contour lines are the same for each contour plot. It can be seen in the figure that the jet velocity, the static pressure, and the total pressure vary widely across the cross-section. In various previous numerical calculations of jets in crossflows [3], either a constant vertical velocity or a constant total pressure was prescribed at the jet exit. The present numerical results, however, show that a significant amount of uncertainty can be caused by the use of either of these boundary conditions at the jet exit.

The calculated velocity vectors, pressure, turbulent kinetic energy, P_r/ε_t, $\varepsilon_t/\varepsilon_p$ and k_p/k_t are shown in Fig. 6. The velocity vector and the pressure contour plots show that the crossflow is decelerated rapidly by the jet and thus the pressure is increased in the forward region of the jet. Otherwise, these plots do not show that any significant phenomena occur in the forward region. The complex P_r/ε_t and $\varepsilon_t/\varepsilon_p$ contours show, however, that the turbulence field is experiencing an enormous evolution in the forward region and that the peak non-equilibrium state occurs along the interface of the jet and the crossflow. The turbulent kinetic energy in the wake region of the jet is far greater than that in the forward region. The turbulence in the forward region is, however, in a stronger non-equilibrium state than that in the wake region. These results indicate that the strength of non-equilibrium turbulence does not necessarily depend on the turbulence intensity. It takes a while for large eddies to cascade to smaller eddies. The large ratio of k_p/k_t in the wake region of the jet is caused by the large eddies convected from the upstream region and those generated in the wake region.

The calculated vertical velocity profiles in the vicinity of the jet exit are compared with the measured data

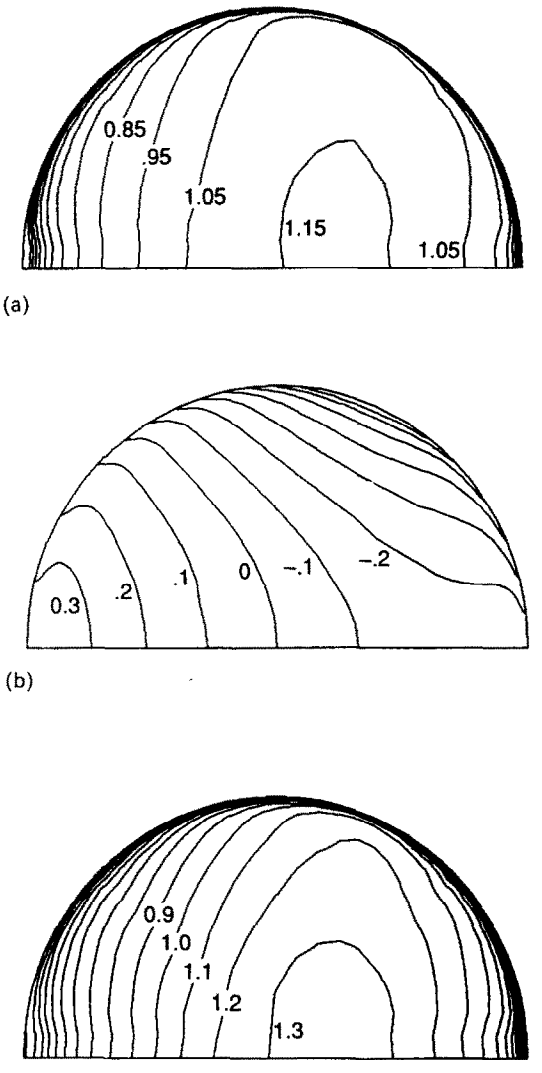

FIG. 5. Contour plots of the flow field at the jet exit, (a) jet velocity, w/W_j, (b) pressure, $p/0.5\rho W_j^2$, (c) total pressure $(p+0.5\rho w^2)/0.5\rho W_j^2$.

in Fig. 7. The under-predicted peak vertical velocity at $z/D = 1.35$ is caused by the coarse grid inaccuracy; otherwise, the calculated vertical velocity profiles are in very good agreement with the measured data.

It is shown in Fig. 8 that the calculated tangential velocity profiles along the x-coordinate direction on the symmetry plane are in good agreement with the measured data. The reversed flow behind the jet indicate that the development of the tangential velocity along the crossflow direction is similar to that of the flow over a circular cylinder. The u-velocity in front of the jet is not, however, brought to zero due to the compliance of the jet.

The calculated turbulent kinetic energy distribution along the x-axis of the symmetry plane at $z/D = 0.75$ is compared with the measured data in Fig. 9. It can be seen in the figure that the trend of the turbulent

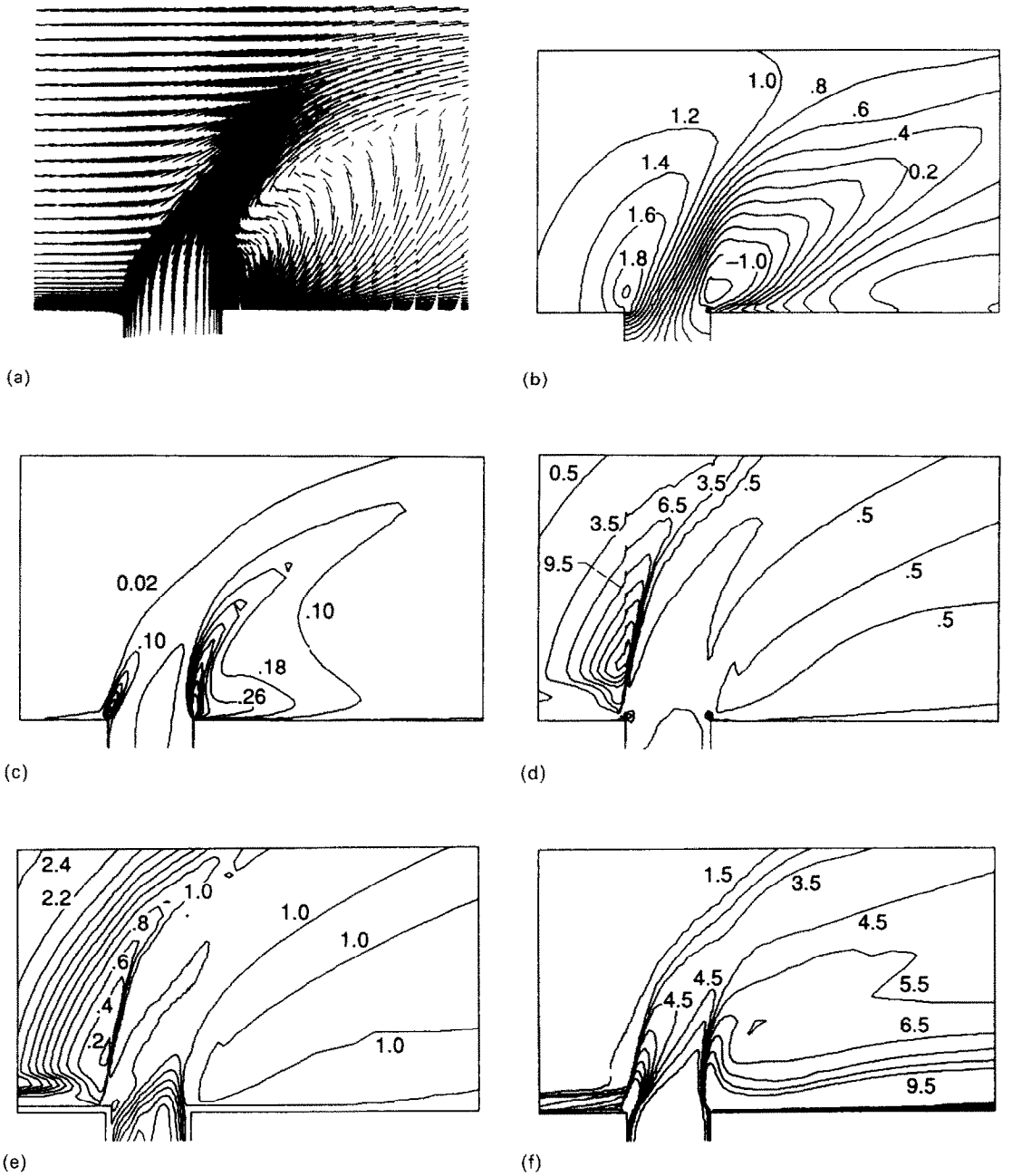

FIG. 6. Flow and turbulence fields on the symmetry plane, (a) velocity vector, (b) pressure, $p/0.5\rho U_0^2$, (c) turbulent kinetic energy ($k/0.5\rho U_0^2$), (d) P_t/ε_t, (e) $\varepsilon_t/\varepsilon_p$, (f) k_p/k_t.

kinetic energy distribution is in excellent agreement with the measured data even though the turbulence intensity is under-predicted.

The calculated concentration profiles at three downstream locations on the symmetry plane are shown in Fig. 10. The shape and the peak locations of the calculated concentration profiles are in very good agreement with the measured data. The slightly smaller magnitude of the concentration is caused by the coarse grid inaccuracy in the far downstream region.

The calculated u-velocity, concentration, and turbulent kinetic energy contours at $x/D = 8$ are shown in Figs. 11(a)–(c), respectively. It can be found in Crabb *et al.* [1] that the present numerical results are in good agreement with the experimentally obtained contour plots. The slight difference between the calculated and the measured u-velocity contour plots in the vicinity of $z/D = 4.5$ is again attributed to the coarse grid inaccuracy in the region. Note that the peak concentration occurs in the region where u-velocity is minimum and that the concentration contour plot exhibits a strong similarity with the turbulent kinetic energy contour plot. This trend is in excellent

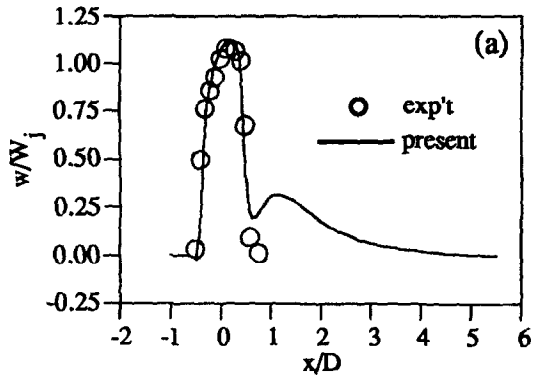

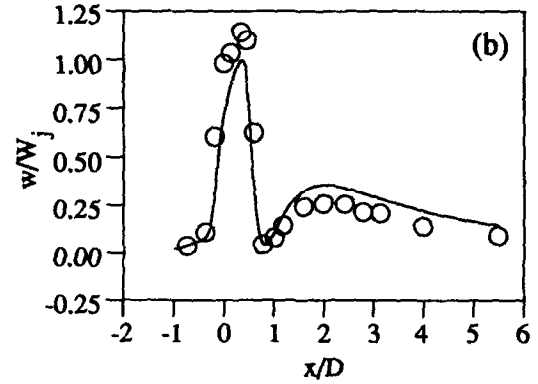

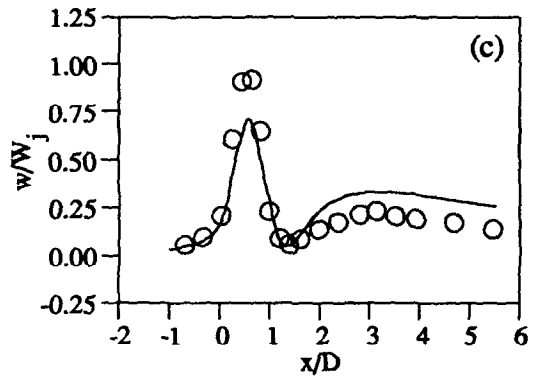

FIG. 7. Vertical velocity (w) profiles on the symmetry plane, (a) $z/D = 0.25$, (b) $z/D = 0.75$, (c) $z/D = 1.35$.

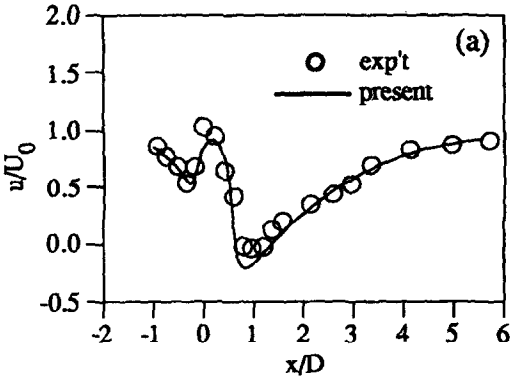

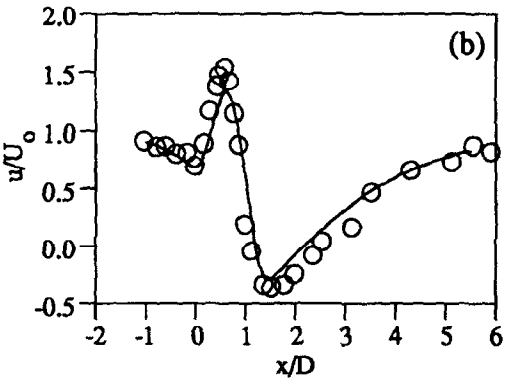

FIG. 8. Tangential velocity (u) profiles on the symmetry plane, (a) $z/D = 0.75$, (b) $z/D = 1.35$.

agreement with the experimentally observed distributions of the concentration and the turbulent kinetic energy and it indicates that the turbulent transport of the concentration is significantly different from that of the mass and momentum.

The three-dimensional particle trajectories are shown in Fig. 12. It can be seen in the figure that the fluid particles passing near the jet exit are most easily entrained to the jet. It is also shown in the figure that the fluid particles near the jet edge carry less momentum and hence these particles are quickly entrained to the helical vortices in the wake region of the jet. The particle trajectories show that the large eddy mixing occurs in the wide region of the jet edge

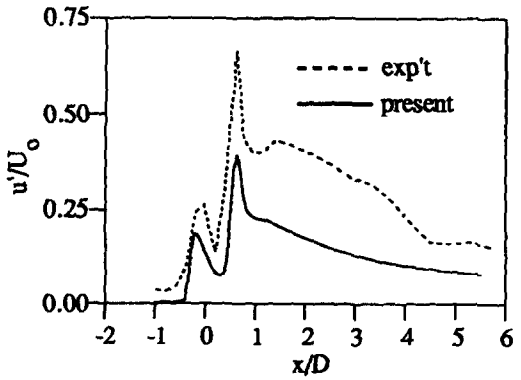

FIG. 9. Turbulent kinetic energy profile on the symmetry plane at $z/D = 0.75$.

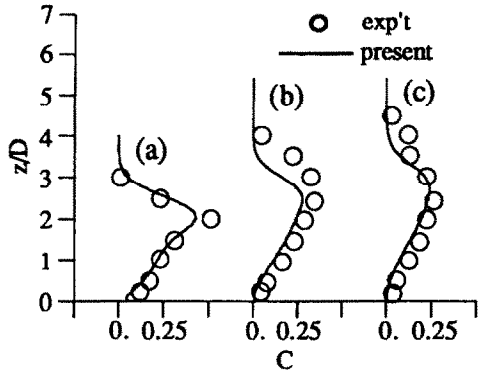

FIG. 10. Concentration profiles at downstream locations on the symmetry plane, (a) $x/D = 4$, (b) $x/D = 6$, (c) $x/D = 8$.

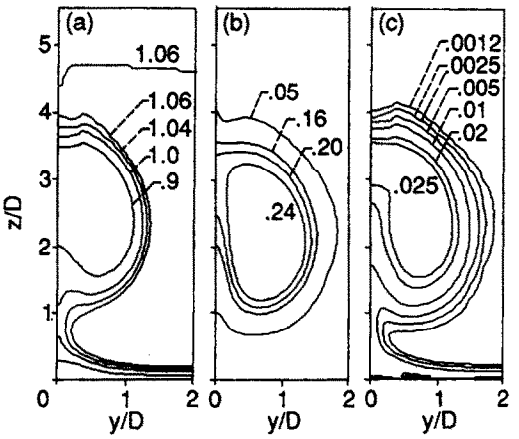

FIG. 11. Contour plots of u-velocity, concentration, and turbulent kinetic energy, (a) u-velocity, (b) concentration, (c) turbulent kinetic energy.

and that the fluid particles in the center region of the jet do not mix easily with the crossflow.

CONCLUSIONS AND DISCUSSION

It is shown that a strong non-equilibrium turbulence field is characterized by the shape and the frequency domain of the spectral density that varies widely in space. The influence of the non-equilibrium turbulence on the developments of the mean fluid flow and the turbulence field can be sensed only through semi-empirical data. The influence of the non-equilibrium turbulence is thus more difficult to recognize than that caused by the turbulence intensity or the anisotropy of turbulence. The significantly improved numerical results for a wide class of complex turbulent flows obtained using the multiple-time-scale turbulence model indicate that the turbulent transport of mass, momentum, and concentration depends strongly on the non-equilibrium turbulence and that the multiple-time-scale turbulence model correctly resolves the non-equilibrium turbulence phenomena.

Numerical results for the circular jet in a crossflow show that the jet and the crossflow interact very strongly with each other in the forward region of the jet and that the interaction creates a strong non-equilibrium turbulence field in the forward region of the jet. The strong interaction between the jet and the crossflow at the jet exit also influences the flow and the turbulence fields in the upstream region of the jet. This result suggests that the upstream region of the circular jet needs to be included in the computational domain in order to obtain accurate numerical results or to assess the predictive capability of a turbulence model. The calculated velocity, concentration, and turbulence fields are in good agreement with the measured data. It is discussed in Crabb *et al.* [1] that the weak vortex shedding does not influence the mean fluid flow significantly. The good comparison between the numerical results and the

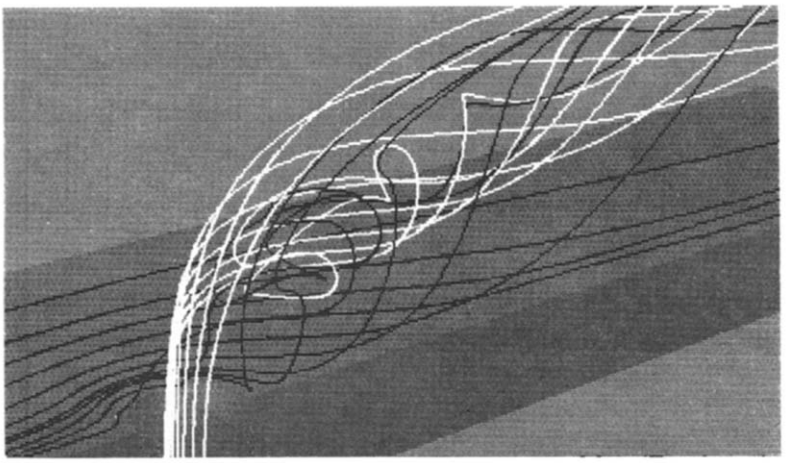

FIG. 12. Three-dimensional particle trajectories.

measured data is also in agreement with such an observation. The calculated tangential velocity, concentration, and turbulent kinetic energy contours at a downstream location show that the peak concentration occurs where the tangential velocity becomes local minimum and that the concentration field exhibits a close resemblance to the turbulence field. This trend is in excellent agreement with that observed in the experiment.

REFERENCES

1. D. Crabb, D. F. G. Durao and J. H. Whitelaw, A round jet normal to a crossflow, *J. Fluid Engng* **103,** 142–152 (1981).
2. Z. A. Khan, Opposed jets in crossflow, Ph.D. thesis, Imperial College of Science and Technology, London (1982).
3. R. W. Claus and S. P. Vanka, Multigrid calculations of a jet in cross flow, AIAA Paper 90-0444 (1990).
4. J. Andreopoulos, Measurements in a jet-pipe flow issuing perpendicularly into a cross stream, *J. Fluid Engng* **104,** 493–499 (1982).
5. S. J. Kline, B. J. Cantwell and G. M. Lilley, The 1980–1981 AFOSR-HTTM *Stanford Conference on Complex Turbulent Flows*, Vol. 1–3, Stanford University, Stanford, California (1981).
6. S.-W. Kim and C.-P. Chen, A multiple-time-scale turbulence model based on variable partitioning of the turbulent kinetic energy spectrum, *Numer. Heat Transfer B* **16,** 193–211 (1989).
7. S.-W. Kim, Numerical investigation of separated transonic turbulent flows with a multiple-time-scale turbulence model, *Numer. Heat Transfer A* **18,** 149–171 (1990).
8. S.-W. Kim, Calculation of reattaching shear layers in divergent channel with a multiple-time-scale turbulence model, *AIAA J.* **29,** 547–554 (1991).
9. S.-W. Kim, Calculations of separated 3-D flows with a pressure-staggered Navier–Stokes equations solver, NASA CR-187065 (1991).
10. P. S. Klebanoff, Characteristics of turbulence in a boundary layer with zero pressure gradient, NACA Report 1247 (1955).
11. I. Wygnanski and H. Fiedler, Some measurements in the self-preserving jet, *J. Fluid Mech.* **3,** 577–612 (1969).
12. K. Hanjelic, B. E. Launder and R. Schiestel, Multiple-time-scale concepts in turbulent shear flows. *Turbulent Shear Flows* (Edited by L. J. S. Bradbury, F. Durst, B. E. Launder, F. W. Schmidt and J. H. Whitelaw), Vol. 2, pp. 36–49. Springer, New York (1980).
13. S. Tavoularis and U. Karnik, Further experiments on the evolution of turbulent stresses and scales in uniformly sheared turbulence, *J. Fluid Mech.* **204,** 457–478 (1989).
14. W. Rodi, The prediction of free boundary layers by use of a two-equation model of turbulence, Ph.D. thesis, University of London, London (1972).
15. B. E. Launder, A generalized algebraic stress transport hypothesis, *AIAA J.* **20,** 436–437 (1982).
16. S.-W. Kim and Y.-S. Chen, A finite element calculation of turbulent boundary layer flows with an algebraic stress turbulence model, *Comput. Meth. Appl. Mech. Engng* **66,** 45–63 (1988).
17. S.-W. Kim, A near-wall turbulence model and its application to fully developed turbulent channel and pipe flows, *Numer. Heat Transfer B* **17,** 101–122 (1990).

CALCUL D'UN JET CIRCULAIRE EN COURANT CROISE AVEC UN MODELE DE TURBULENCE A ECHELLE DE TEMPS MULTIPLE

Résumé—On présente le calcul de l'écoulement turbulent tridimensionnel d'un jet dans un courant croisé avec un modèle de turbulence à échelle de temps multiple. La turbulence dans la région amont du jet est en état de déséquilibre plus prononcé que dans la région de sillage, tandis que le niveau de turbulence dans le sillage est plus élevé. L'écoulement calculé ainsi que le champ de concentration sont en très bon accord avec les mesures expérimentales et cela indique que le transport turbulent de masse, de concentration et de quantité de mouvement est fortement gouverné par la turbulence hors d'équilibre. L'aptitude du modèle de turbulence à échelle de temps multiple à résoudre le champ de turbulence hors-équilibre est aussi discutée.

BERECHNUNG EINES QUER ANGESTRÖMTEN KREISFÖRMIGEN STRAHLS MITTELS EINES TURBULENZMODELLS MIT MEHRFACHER ZEITSKALIERUNG

Zusammenfassung—Es wird die Berechnung der dreidimensionalen turbulenten Strömung in einem quer angeströmten Strahl vorgestellt, bei der ein Turbulenzmodell mit mehrfacher Zeitskalierung verwendet wird. Die Turbulenz im Anströmbereich des Strahls ist stärker im Nichtgleichgewichtszustand als diejenige im Abströmbereich während der Turbulenzgrad im Abströmbereich größer ist als derjenige an der Vorderseite. Die berechnete Strömung und das Konzentrationsfeld stimmen gut mit Versuchsdaten überein, und es zeigt sich, daß der turbulente Massen-, Konzentrations- und Impulstransport stark von der Nichtgleichgewichtsturbulenz beeinflußt wird. Es wird zusätzlich die Möglichkeit diskutiert, mit Hilfe eines Turbulenzmodells mit mehrfacher Zeitskalierung das Nichtgleichgewichts-Turbulenz-Feld zu berechnen.

РАСЧЕТ КРУГЛОЙ СТРУИ ПРИ ПОПЕРЕЧНОМ ОБТЕКАНИИ С ИСПОЛЬЗОВАНИЕМ МОДЕЛИ ТУРБУЛЕНТНОСТИ С МНОЖЕСТВЕННЫМИ ВРЕМЕННЫМИ МАСШТАБАМИ

Аннотация—Приводится расчет трехмерной турбулентной струи при поперечном обтекании с использованием модели турбулентности с множественными временными масштабами. На переднем участке струи турбулентность является более неравновесной, чем в области следа, в то время как уровень турбулентности в области следа выше, чем на переднем участке. Рассчитанные поля течения и концентраций очень хорошо согласуются с данными измерений, что свидетельствует о сильной зависимости турбулентного переноса массы, концентрации и импульса от неравновесной турбулентности. Обсуждается возможность определения поля неравновесной турбулентности с помощью предлагаемой модели.